Science Arts & Métiers (SAM)

Tailoring interfacial properties of 3D-printed continuous natural fiber reinforced polypropylene composites through parameter optimization using machine learning methods

Ruijun Cai [a], Wei Wen [b], Kui Wang [a,*], Yong Peng [a], Said Ahzi [c], Francisco Chinesta [d]

[a] *Key Laboratory of Traffic Safety on Track of Ministry of Education, School of Traffic & Transportation Engineering, Central South University, Changsha 410075, China*
[b] *Department of Engineering, Lancaster University, Lancaster LA1 4YR, UK*
[c] *ICUBE Laboratory-CNRS, University of Strasbourg, Strasbourg 67000, France*
[d] *ESI Chair, PIMM, Arts et Métiers Institute of Technology, Paris 75013, France*

ARTICLE INFO

ABSTRACT

3D-printed continuous ramie fiber reinforced polypropylene composites (CRFRPP) are expected to ensure good mechanical properties while meeting the requirements of environmental friendliness and sustainability. To promote the wide industrial application of CRFRPP, this work investigated the effects of printing parameters (extrusion flow rate, printing temperature, layer thickness and printing speed) on the interfacial properties of CRFRPP. The interlayer and intralayer interfacial properties of CRFRPP with different printing parameters were studied using the design of experiment approach. Machine learning methods and response surface methodology prediction were also carried out based on the experimental results to bridge the printing parameters and interfacial properties. According to the prediction results, the printing parameters were optimized to improve the production efficiency while ensuring the desired interfacial performance. At last, the bending tests were conducted to investigate how the difference in interfacial properties can be translated to the mechanical performance. The results found that printed specimens with weak interfacial strength suffered interlaminar delamination failure when subjected to bending loads, greatly weakening the mechanical properties of the composites.

1. Introduction

Additive manufacturing (AM), also known as 3D printing, is a promising manufacturing technology for quickly and cost-effectively fabricating objects with complicated structures [1]. Material extrusion-based additive manufacturing (ME-AM) is a widely used AM method that fabricated 3D parts by selectively laying extruded semi-molten thermoplastic materials. ME-AM has attracted increasing attention due to its advantages of simple process, cost-saving, high forming efficiency and multi-material flexibility [2]. However, some challenges, such as voids in the microstructure and poor interfacial interaction, impact negatively the mechanical properties of printed parts thus limiting the industrial application of ME-AM products [3]. Driven by these challenges and applications, polymer-based particles, short fiber and continuous fiber reinforced composites have been intensively investigated to improve the properties of the printed parts. Among these composites, continuous fiber reinforced composites usually outperform particles and short fiber reinforced composites in terms of mechanical performance [3–5]. The current literature mainly focused on 3D-printed continuous synthetic fibers reinforced composites [6,7]. However, the extensive use of non-biodegradable synthetic fiber materials would affect negatively the environment [8]. Taking into account the needs of environmental friendliness and sustainable development, natural fibers were suggested as the replacement for synthetic fibers [8,9].

Continuous natural fiber reinforced composite prepared by ME-AM is still a young field of research with limited works in the literature available. Matsuzaki et al. [10] fabricated jute reinforced polylactic acid (PLA)-based composites by in-situ impregnation 3D printing method and investigated their tensile properties. It was found that the tensile modulus and strength of the continuous jute reinforced PLA printed specimen increased by 157 % and 134 %, respectively, compared with those of the 3D-printed neat PLA specimens. Le Duigou et al. [11]

investigated the tensile properties of ME-AM fabricated continuous flax fiber reinforced PLA composites. The results showed that the longitudinal tensile modulus and strength of continuous flax fiber reinforced PLA composites were improved by a factor of 4.5. In another work of Le Duigou et al. [12], the mechanical properties of 3D-printed continuous flax/PLA biocomposites were demonstrated to be very sensitive to the printing parameters such as layer thickness and interfilament distance. Cheng et al. [6] investigated the effects of printing parameters on interfacial and tensile mechanical properties of continuous ramie fiber reinforced PLA fabricated by ME-AM. The results indicated that the interfacial and tensile mechanical properties of the printed ramie/PLA composites increased as increasing printing temperature and decreasing layer thickness as well as printing speed.

It can be seen that PLA as the matrix of continuous natural fiber reinforced composites is getting more attention due to its facile processability and biodegradability. However, PLA was severely limited by its relatively low toughness and poor heat resistance [13,14]. In recent years, PP has emerged as a new 3D printing material due to its heat stability and excellent balance between toughness and rigidness [15]. Moreover, PP had superior remanufacturing capacity among various commercially available 3D printing materials [16]. Therefore, 3D-printed continuous natural fiber reinforced PP composites have promising potential to be environment-friendly and sustainable composites with good mechanical properties.

As previously stated, the mechanical behaviors of 3D-printed continuous fiber reinforced composites highly depended on the printing parameters. In the available studies, the effects of process parameters on the mechanical properties of 3D-printed continuous natural fiber reinforced composites were mainly studied experimentally. However, the experimental methods are time-consuming and costly when considering many parameters and their interactions. Although finite element and theoretical modeling could also be applied to study properties of material and structure, their inherent physical assumptions and high computational costs make them challenging to analyze 3D-printed composites with complex microstructures [17–20]. In addition, when interrelated variables are presented in a nonlinear pattern, it is difficult to reveal their relationships using traditional methods [19,21]. The application of data-driven methods, such as machine learning (ML), may provide effective solutions for the above issues. In fact, ML method has been applied to AM with promising results in recent years [19,21–27].

In this work, continuous ramie fiber reinforced PP composites (CRFRPP) were prepared by in-situ impregnation 3D printing. Interfacial (interlayer and intralayer) properties of CRFRPP were investigated as they may impact significantly on the mechanical properties of 3D-printed composites [28–33]. Effects of printing parameters such as extrusion flow rate, printing temperature, layer thickness and printing speed on the interfacial properties of CRFRPP were studied. Box-Behnken design (BBD) and factorial design methods were combined to design experiments with the consideration of reflecting the interaction among parameters as much as possible. Response surface methodology (RSM) was applied to predict interlayer and intralayer adhesion properties of CRFRPP with different printing parameters. In addition, two ML algorithms, random forest (RF) and artificial neural network (ANN) were also applied to build prediction models of interfacial properties. The performance of the above methods was evaluated. Parameters were optimized based on the prediction results given by the prediction model with the best performance. At last, the bending tests were conducted to investigate how the difference in interfacial properties can be translated to the mechanical performance.

2. Experiments and modeling

2.1. Materials and processing

In this work, commercial talc (12 wt%) filled and ethylene-propylene-diene-monomer (EPDM) (20 wt%) toughened commercial PP-based composite, PP/EPDM/talc (grade 7510, Sabic, Saudi Arabia), was selected to be the matrix for CRFRPP. Continuous ramie fiber (Hunan Huasheng Dongting Ramie Textile co., ltd, Hunan, China) was selected to be the reinforcement for CRFRPP in this study. This ramie yarn was twisted (400 turn/meter) with a linear density of 36 Nm/2R. Nm is an indirect yarn count system. The length of yarn in meters of one gram of yarn or the length of yarn in kilometers of one kilogram of yarn is called new metric count (Nm). 2R means that the number of strands plied together in the yarn is 2.

The as-received granular PP/EPDM/talc material was first dried in an oven at 80 °C for one hour and then extruded using a twin-screw extruder at a final die temperature of 185 °C. The filament was extruded evenly by the extruder, keeping a stable diameter of 1.75 mm. The ramie yarns were also dried in an oven at 80 °C for two hours before the 3D printing process. 3D printer allowing in-situ impregnation (Combot-200, Fibertech, Shanxi, China) with a single 1.3 mm diameter flat-head nozzle was applied to fabricate CRFRPP samples in this work. As shown in Fig. 1(a), during the printing process, PP filament was fed into a liquefier to heat and melt. Then the ramie yarn was impregnated with molten PP in the liquefier and together extruded by the nozzle. Under the action of heat and pressure, adjacent extruded filaments within the layer were bonded and then adjacent layers were bonded. The intralayer and interlayer adhesion strengths were denoted as Intra-Strength and Inter-Strength in this study, respectively, as shown in Fig. 1(b). The extruded filament was deposited in a rectilinear pattern.

2.2. Characterization

Four printing parameters that could have great influences on the performance of the printed specimen: extrusion flow rate, printing temperature, layer thickness and printing speed were chosen to study their effects on the interfacial properties of CRFRPP, and each parameter was set at three levels, as shown in Table 1. Note that the extrusion flow rate was the parameter from the slicing software, which meant the extrusion amount of molten resin in unit length, the greater value of it represented the more resin extrusion per unit length. The print line spacing was set at a constant value of 1.0 mm to ensure printed specimens can be successfully printed under all printing parameters combinations in our work. Box-Behnken design (BBD) was used to generate experimental points in this study. For BBD, only tests in the center points were designed to repeat for evaluating the error of experiments [34–36]. In addition, we added 12 experimental points to better train and validate ML models for improving prediction accuracy. As a result, each type of test (Inter-strength or Intra-strength test) had 39 experimental points and 78 tests were conducted in total.

The combinations of printing parameters based on the experimental design as well as the experimental results are detailed in Section 3.1 (shown in Table 3). According to the experimental design, CRFRPP with different printing parameter combinations were manufactured and their interfacial properties (interlayer and intralayer adhesion properties) were examined. Inspired by these works [32,37–43] and ASTM D1938
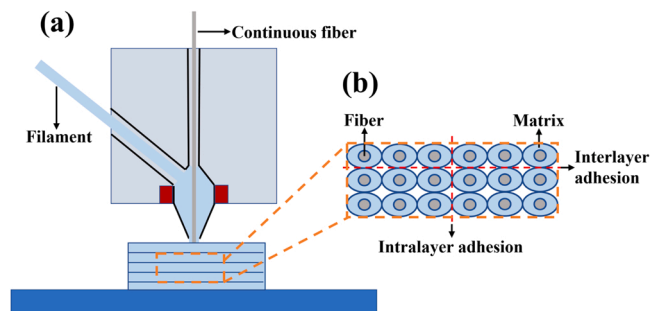

Fig. 1. Schematic of the (a) in-situ impregnation 3D printing process (b) cross-section of the printed specimen.

Table 1
Printing parameters with their codes and levels.

Printing parameters	Codes	Levels		
		Low level	Center level	High level
Extrusion flow rate (%)	E	50	70	90
Printing temperature (°C)	T	190	210	230
Layer thickness (mm)	L	0.30	0.45	0.60
Printing speed (mm/min)	V	100	300	500

standard, interlayer and intralayer adhesion strengths (Inter-Strength and Intra-Strength) of CRFRPP were characterized by the means of methods shown in Fig. 2 using a universal mechanical testing machine (E44, MTS Co., USA). For Inter-Strength characterization, the test specimens with a length of 80 mm and a width of 6 mm were printed as three layers, as shown in Fig. 2(a). For Intra-Strength characterization, the test specimens with a length of 80 mm and a width of 6 mm were printed as two layers, as shown in Fig. 2(b). Fig. 2(c) shows the typical curve for an Inter-Strength measurement (curves for Intra-Strength measurement showed similar trends therefore were not presented). Interlayer and intralayer adhesion forces were obtained from the average of the steady-state region. Then interlayer and intralayer adhesion forces were normalized by width of Inter-Strength test specimen and thickness of Intra-Strength test specimen, respectively.

To investigate how the interfacial properties influence the mechanical performance of printed specimen, three-point bending tests were carried out using the universal mechanical testing machine. The bending tests were performed with a constant cross-head speed of 3 mm/min and at room temperature according to ISO14125. The bending test specimen was cuboid with dimensions of 90 mm × 6 mm × 6 mm.

The morphological properties of the specimens after Inter-Strength and Intra-Strength tests were investigated using an optical microscope (OM) (AO-3M150GS, AOSVI, Shenzhen, China).

2.3. Modeling and evaluation

Three methods, response surface methodology (RSM), random forest (RF) and artificial neural network (ANN), were selected as prediction models. These two ML models were developed using Python (Python Software Foundation). Scikit-learn (scikit-learn package, v0.24.2) [44], an open-source ML library for Python, was used to execute ML algorithms in this study.

The dataset used for modeling was built based on the experimental results. Here, the inputs for the models were extrusion flow rate, printing

temperature, layer thickness and printing speed. And the outputs were corresponding Inter-Strength and Intra-Strength. The data were randomly divided into training and test datasets in the ratio of 9:1, which were used to calibrate the model and validate the results of the training protocol, respectively. For each ML method, hyperparameters were fine-tuned by empirical methods, grid search techniques and references to related literature [22,45] to maximize model performance. The optimized hyperparameters are shown in Table 2. A brief explanation of the meanings for all hyperparameters mentioned in this study was presented in the Supplementary material.

Four metrics were used to evaluate the accuracy of the prediction. These four metrics were R^2, Mean Absolute Error (MAE), Root Mean Square Error (RMSE) and Median Absolute Error (MedAE). The equations and brief explanations of these metrics were presented in the Supplementary material.

3. Results

3.1. Experimental results

Table 3 shows the Inter-Strength and Intra-Strength of the CRFRPP under different printing parameters. These results would be used as training and test datasets for ML models. It should be mentioned that Inter-Strength and Intra-Strength derived from the interlayer and intralayer adhesion forces normalized by width of Inter-Strength test specimen and thickness of Intra-Strength test specimen, respectively, so their units are N/cm.

In order to show clearly the variation trends of the Inter-Strength and Intra-Strength of printed parts as a function of printing parameters, experimental results are presented in Fig. 3. Note that for BBD, only tests in the center points were designed to repeat for evaluating the error of

Table 2
Optimized hyperparameters for machine learning methods in this study.

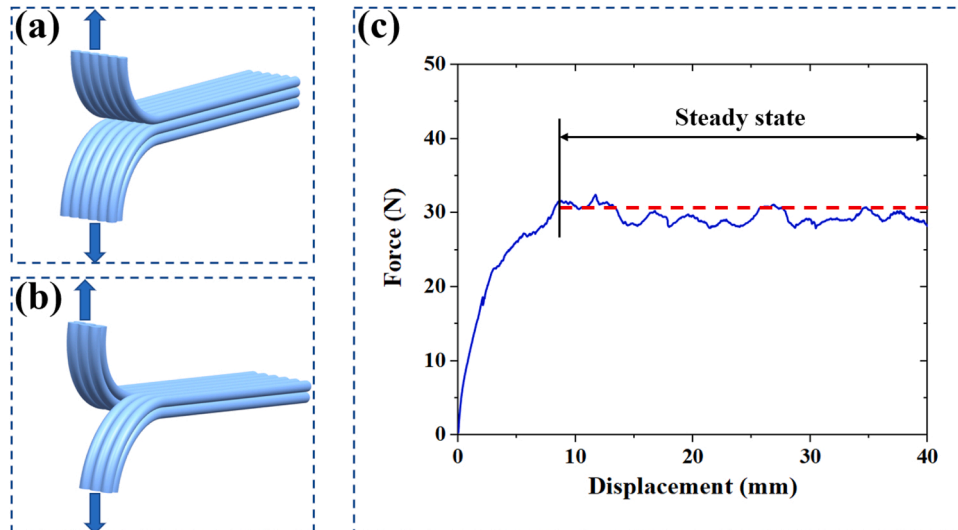| Method	Method hyperparameters	Best parameters
RF	max_depth	4
	min_samples_leaf	1
	min_samples_split	2
	n_estimators	50
	solver	lbfgs
	activation	tanh
	hidden_layer_sizes	(4,3,3,1)
ANN	Max_iter	134

Fig. 2. Schematic of the (a) Inter-Strength and (b) Intra-Strength tests, and (c) typical curve for Inter-Strength measurement.

l.

Table 3
Inter-Strength and Intra-Strength of the CRFRPP under different printing parameters.

Tests	Extrusion flow rate (%)	Printing temperature (°C)	Layer thickness (mm)	Printing speed (mm/min)	Inter-Strength (N/cm)	Intra-Strength (N/cm)
1	50	210	0.45	500	12.56	40.61
2	90	210	0.45	100	29.34	110.38
3	70	230	0.45	100	24.70	113.67
4	70	210	0.6	500	9.69	67.68
5	70	210	0.45	500	14.30	72.79
6	50	230	0.45	300	18.15	68.67
7	90	210	0.45	300	32.34	103.43
8	70	230	0.60	300	20.49	78.04
9	70	190	0.45	100	3.57	34.10
10	70	230	0.45	500	25.31	83.29
11	90	230	0.45	300	35.67	105.05
12	70	230	0.30	300	27.22	117.58
13	70	210	0.45	300	12.17	67.39
14	70	210	0.45	300	12.65	64.67
15	70	190	0.30	300	9.24	54.02
16	70	210	0.60	100	9.61	53.02
17	50	210	0.45	300	11.45	50.44
18	70	210	0.60	300	9.71	59.67
19	70	190	0.45	500	11.93	35.10
20	90	210	0.45	300	30.00	100.79
21	90	210	0.60	300	26.16	80.49
22	70	210	0.45	100	11.93	64.59
23	90	190	0.45	300	23.38	82.20
24	70	210	0.30	500	15.53	67.73
25	90	210	0.45	500	29.59	101.59
26	70	230	0.45	300	25.65	93.89
27	70	210	0.30	300	14.09	94.70
28	70	190	0.60	300	1.10	16.75
29	70	190	0.45	300	8.45	49.54
30	50	190	0.45	300	1.83	14.39
31	50	210	0.60	300	1.85	40.81
32	70	210	0.45	300	12.61	70.09
33	50	210	0.45	300	11.82	48.79
34	70	210	0.30	100	15.79	72.38
35	70	210	0.45	500	13.44	62.53
36	50	210	0.30	300	13.86	52.02
37	90	210	0.30	300	39.21	120.35
38	50	210	0.45	100	9.94	58.98
39	70	210	0.45	100	12.06	65.23
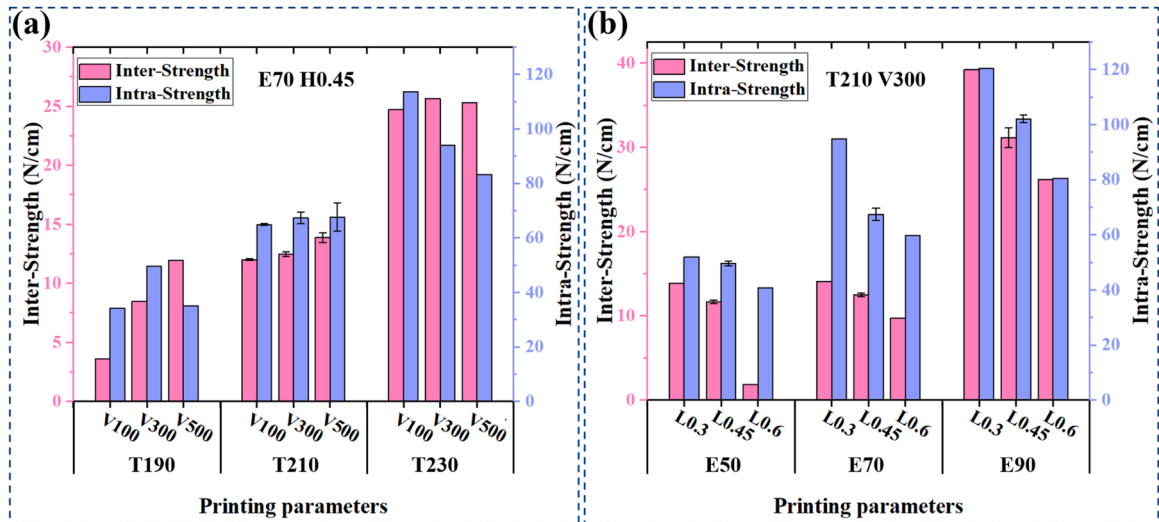
Fig. 3. Inter-Strength and Intra-Strength of the CRFRPP under different printing parameters.

experiments, therefore only these results had error bars. In Fig. 3(a), it can be found that when the printing temperature was 190 °C, Inter-Strength increased with the increase of printing speed. However, when printing temperature was 210 °C and 230 °C, it seemed that printing speed had an insignificant effect on the Inter-Strength of CRFRPP. Similarly, the change of Intra-Strength as a function of printing

speed also presented different trends under different printing temperatures. In Fig. 3(b), it can be seen that when printing temperature and printing speed were at their center level, the Inter-Strength and Intra-Strength of CRFRPP under three extrusion flow rates decreased with the increase of layer thickness and the degree of decline was different under different extrusion flow. The interactions between printing

parameters were obvious and discrete experimental results showed nonlinear and complex rules. Therefore, they were combined with the prediction models to know the overall rules, which were necessary for the optimization.

3.2. Evaluation results of models

Fig. 4 shows the R^2 score and error (MAE, RMSE, MedAE) of the prediction models for Inter-Strength and Intra-Strength. In Fig. 4(a), it can be seen that all three prediction models for Inter-Strength showed higher R^2 scores. However, for Intra-Strength, RSM presented a relatively lower R^2 score. In addition, ANOVA results (see in Tables S1 and S2 in the Supplementary material) found that for both Inter-Strength and Intra-Strength, the Lack of Fit of RSM was significant, which meant the fit of RSM to actual results was significantly inaccurate. Besides, RF presented an acceptable R^2 score (above 0.9) and ANN showed the highest R^2 score as expected. In addition, the R^2 score on the training dataset and test dataset were also calculated to evaluate whether the ANN model was over-fitting. If the model presented a high R^2 score on the training dataset but a low R^2 score in the test dataset, it meant that overfitting occurred during the training process, indicating poor generalizability of the models. In this study, for Inter-Strength, the R^2 of ANN model on the training and test dataset were 0.9682 and 0.9677, respectively. And for Intra-Strength, the R^2 of ANN model on the training and test dataset were 0.9449 and 0.9513, respectively. It was found that the R^2 of the ANN model on the training set was not significantly bigger than that on the test set. Therefore, there seemed to be no obvious overfitting phenomenon in this work.

The R^2 score is an intuitive way to evaluate the performance of each model on the dataset, but it cannot directly quantify the error for specific data. To directly measure the practicality of the model for the problem, errors between predicted values and actual values were also used for model evaluation, as shown in Fig. 4(b). It can be found that among the three models, ANN had the lowest errors for both Inter-Strength and Intra-Strength predictions.

3.3. Predicted results

Fig. 5 presents the ANN prediction results because ANN prediction results had the highest accuracy. Note that the step sizes of the printing parameters for the predicting dataset were: E: 5 %, T: 5 °C, L: 0.05 mm, and V: 50 mm/min. Only part of the results was shown here as they were sufficient to show the major effects of printing parameters on Inter-Strength and Intra-Strength of CRFRPP. In Fig. 5(a), it can be found that when layer thickness and printing speed were at their center level, the Inter-Strength of CRFRPP increased with the increase of extrusion

flow rate and printing temperature (Similar trends can be found when the layer thickness and printing speed in their other levels). In addition, when the extrusion flow rate was low, as increasing printing temperature, the Inter-Strength of CRFRPP was significantly improved. However, when the extrusion flow rate was high, CRFRPP with moderate printing temperature also had high Inter-Strength. In Fig. 5(b), it can be found that when printing temperature and printing speed were at their center level, the Inter-Strength of CRFRPP decreased with the increase of layer thickness. In addition, when the extrusion flow rate was low, with increasing layer thickness, the Inter-Strength of CRFRPP significantly decreased. However, when the extrusion flow rate was high, CRFRPP with relatively high layer thickness also had high Inter-strength. Intra-Strength presented similar trends as mentioned above under the same printing temperature so they were not shown here. In Fig. 5(c), it can be seen that when extrusion flow rate and layer thickness were at their center level, printing speed had an insignificant influence on the Inter-Strength of CRFRPP. However, at high printing temperature, the Intra-Strength of CRFRPP decreased with the increase of printing speed as shown in Fig. 5(d). The above results indicated that good interfacial performance of CRFRPP could be achieved without having to set each print parameter to its highest or lowest value, providing the possibility of multi-objective optimization.

3.4. Parameter optimization results

To ensure the high Inter-Strength and Intra-Strength of CRFRPP and improve forming efficiency, based on the ANN prediction results, printing parameters were optimized according to the following principles:

(1) Good Inter-Strength and Intra-Strength of CRFRPP: through adjusting printing parameters, the Inter-Strength and Intra-Strength of CRFRPP could be set as a percentage of their maximum value (in their prediction results range), or as a multiple of the mean or median, depending on practical needs.
(2) Low forming time: on the basis of satisfying the first principle, the printing parameters that led to the least forming time should be selected. In this study, the forming time of printed specimens was given by the slicing software and was related to the printing speed and layer thickness.
(3) Low energy cost: after satisfying the above two principles, if the available parameters were not a unique combination, then a set of parameters with relatively low printing temperatures should be selected to save energy.

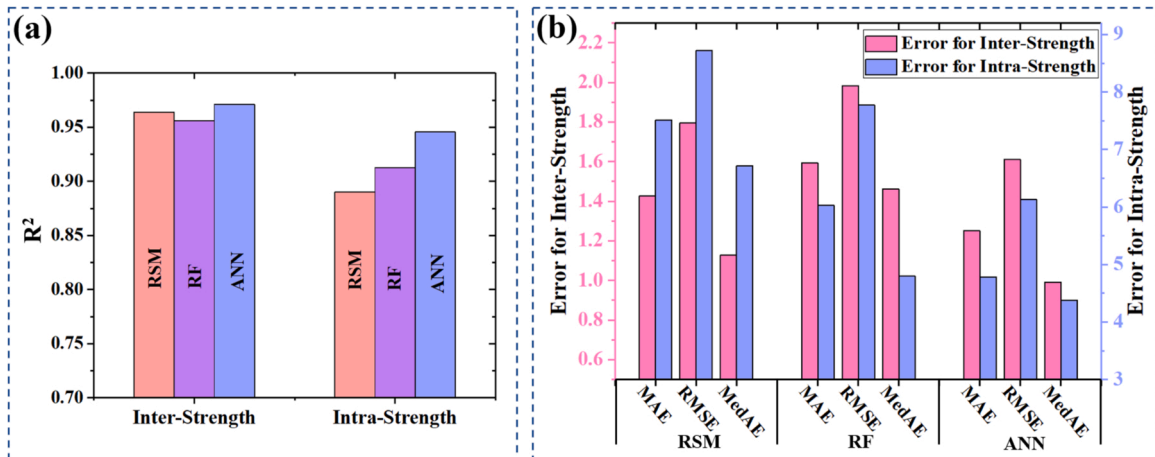For example, to print 50 mm × 50 mm × 50 mm solid cube

Fig. 4. (a) R^2 score and (b) errors (MAE, RMSE, MedAE) of the prediction models for Inter-Strength and Intra-Strength.
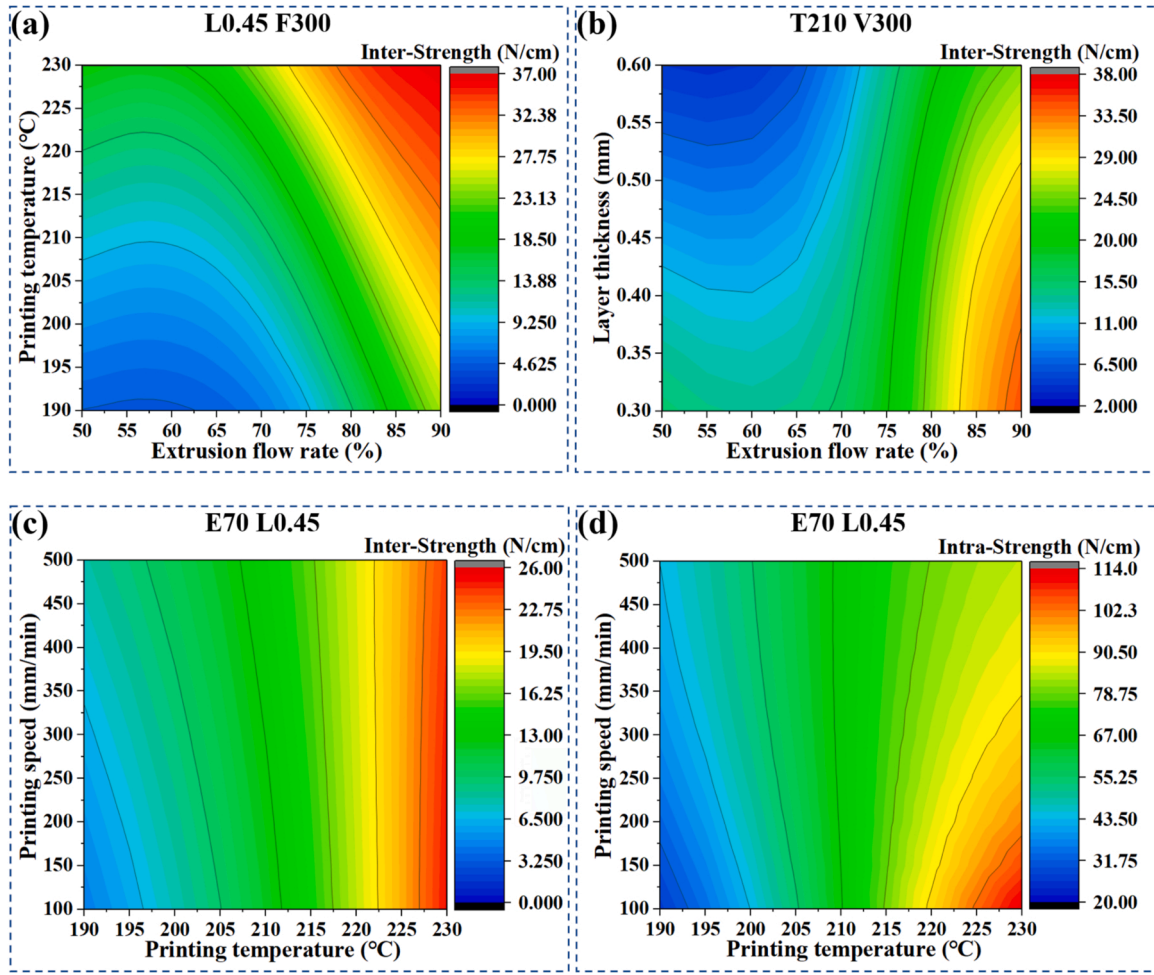
Fig. 5. Inter-Strength and Intra-Strength of CRFRPP under different printing parameters.

specimen (printed parts with other sizes and shapes also could be chosen according to actual needs), if both Inter-Strength and Intra-Strength of CRFRPP were set above 95 %, 90 %, 85 %, 80 %, 75 % and 70 % of their

nonlinear and interactive interactions between parameters. This may be the reason why RSM performs poorly in Intra-Strength prediction.

$$
\begin{aligned}
\mathrm{Inter-Strength} = {} & 108.84955 - 1.24548E - 1.14408T - 23.56785L + 0.11136V - 0.002522E * T - 0.086167E * L - 0.000148E * V + 0.117417T \\
& * L - 0.000484T * V + 0.002750L * V + 0.016940E * E + 0.004365T * T - 25.245647L * L + 7.217331V * V
\end{aligned}
\tag{1}
$$

maximum values (these thresholds were denoted as Td), the optimized parameters were listed in Table 4.

4. Discussion

4.1. Comparison of models

As the results discussed in Figs. 3 and 5, the variation of Intra-Strength as a function of printing parameters showed more nonlinear and complex rules than those of Inter-Strength, which would be a possible reason that all three Intra-Strength prediction models presented a relatively low R^2 score. As a multiple regression method, RSM can give linear or non-linear models, and each model was scored for accuracy. Eq. (1) and (2) are the highest-scoring models from RSM. In Eq. (1), it can be seen that the model for Inter-Strength prediction is a nonlinear regression equation considering the interaction between parameters, whereas the model for Intra-Strength prediction in Eq. (2) failed to achieve the

$$
\begin{aligned}
\mathrm{Intra-Strength} = {} & -261.44119 + 1.34246E + 1.336071T - 86.82048L \\
& - 0.01282V
\end{aligned}
\tag{2}
$$

Table 4
Optimized parameters for different setting percentages (Td) of their maximum values of Inter-Strength and Intra-Strength.

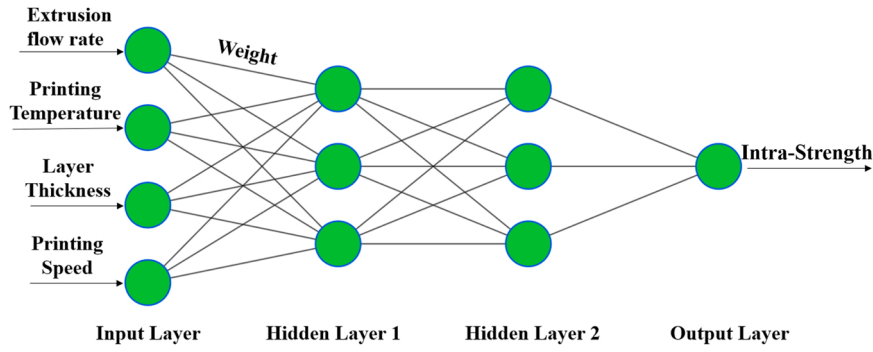| Td (%)	E (%)	T (°C)	L (mm)	V (mm/ min)	Inter-Strength (N/cm)	Intra-Strength (N/cm)	Forming time (h)
95	90	225	0.30	150	38.23	136.84	45.37
90	90	220	0.30	250	37.32	129.63	27.18
85	90	215	0.30	400	36.43	122.19	17.22
80	90	215	0.35	450	35.97	113.93	13.28
75	90	215	0.40	450	35.19	107.66	11.65
70	90	210	0.45	500	33.13	99.71	9.45

Fig. 6. Schematic graph of the structure of ANN prediction model for Intra-Strength.

Fig. 6 shows the schematic graph of the structure of the ANN prediction model for Intra-Strength in this work. The ANN structure in this study comprises one input layer, two hidden layers and one output layer, and each layer contains some neurons. Neurons in two neighboring layers are linked, and the magnitudes of the links between neurons in two adjacent layers are referred as "weight" [46]. The difference between the expected and true output values was utilized to change the weight for increasing accuracy. The error usually gets smaller after a few iterations. As a result, ANN could capture the complicated and nonlinear relationship between the parameters and Intra-Strength, which was the reason why ANN had the best performance for Intra-Strength prediction.

Although RF did not perform as well as ANN, it also gave an acceptable R^2 score (above 0.9). Moreover, its main advantage is that it can output the importance of parameters, which can evaluate what extent a given printing parameter influences the Inter-Strength and Intra-Strength from a holistic point of view. The importance of parameters will be discussed in detail in the next section.

4.2. Effects of printing parameter on the interfacial properties

Fig. 7 shows the importance of four printing parameters. It can be found that extrusion flow rate (E) had the most important influence on both Inter-Strength and Intra-Strength. And printing speed (V) had a relatively small influence on both Inter-Strength and Intra-Strength. For Intra-Strength, printing temperature had close importance compared to extrusion flow rate. One parameter with higher importance should be considered firstly in the adjustment to obtain better properties. For example, in this study, to obtain higher Inter-Strength and Intra-Strength, the first and most important thing is to select the appropriate extrusion flow rate, followed by adjusting the printing

temperature and layer thickness, and finally to consider adjusting the printing speed. In addition, one parameter with higher importance indicated it has a relatively narrow parameter selection window. For example, as the optimized results in Table 4, when Inter-Strength and Intra-Strength of CRFRPP were set above from 95 % to 70 % of their maximum value, all optimized extrusion flow rates were 90 %.

Fig. 8 shows the typical fracture surfaces of CRFRPP after Inter-Strength and Intra-Strength tests. In Fig. 8(a), it can be found that interlayer debonding contained fiber/matrix debonding (as shown in area 1) and matrix/matrix debonding (as shown in area 2). In Fig. 8(b), the debonding between the fine ramie fiber branches of yarns and resin (as shown in area 3) and debonding between resin and resin can be seen (as shown in area 4). Therefore, both the adhesion strength of interlayer resin and the degree of impregnation of fiber had important influence on the interlayer interaction.

Fig. 9 shows the fracture surfaces of CRFRPP under different printing parameters. Note that the fracture surfaces in which fibers can be seen after Inter-Strength tests (similar to the right image in Fig. 8(a)) were not presented here because their difference was less visible compared with the fracture surfaces in which fibers were hard to be seen after Inter-Strength tests (just like the left image in Fig. 8(a)). The interface morphologies at different printing speeds showed limited differences and therefore were not presented here. As shown in Fig. 9(a) and (g), at a given printing temperature of 190 °C, when the extrusion flow rate was low, obvious voids between filaments could be seen. These defects could seriously decrease the Intra-Strength of CRFRPP. As a result, the Intra-Strengths of CRFRPP at lower extrusion flow rates and lower printing temperatures were significantly inferior to those at higher extrusion flow rates and higher printing temperatures (see Figs. 3 and 5). Comparing to Fig. 9(a) with (c), more and obvious defects can be seen in
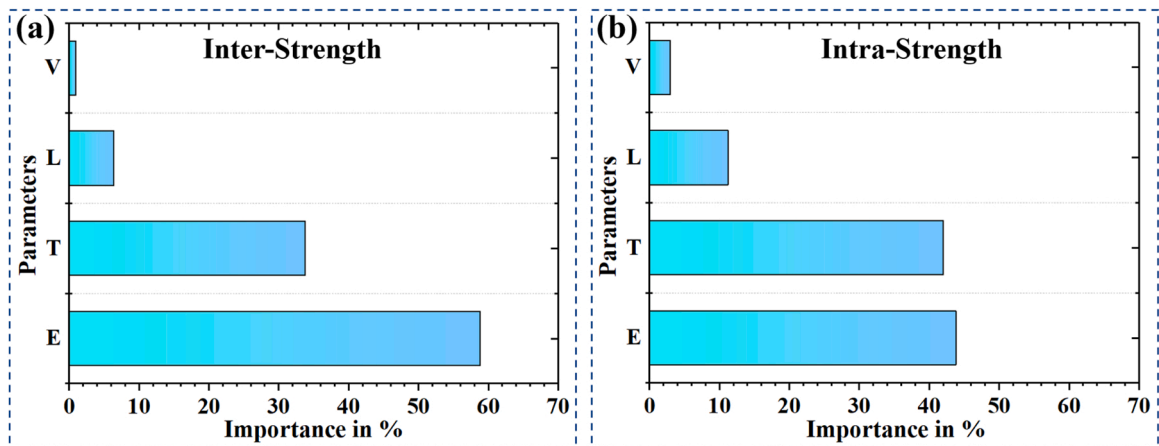

Fig. 7. The importance of four printing parameters, which can evaluate to what extent a given printing parameter influences the Inter-Strength and Intra-Strength from a holistic point of view.
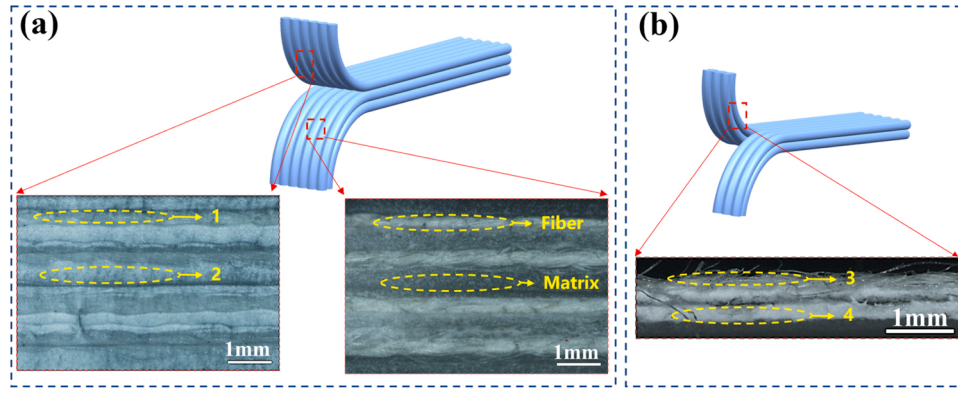
Fig. 8. Typical fracture surfaces of CRFRPP after (a) Inter-Strength and (b) Intra- Strength tests, in which, area 1 is fiber/matrix debonding, area 2 is matrix/matrix debonding, area 3 is the debonding between the fine ramie fiber branches of yarns and resin and area 4 is debonding between resin and resin.
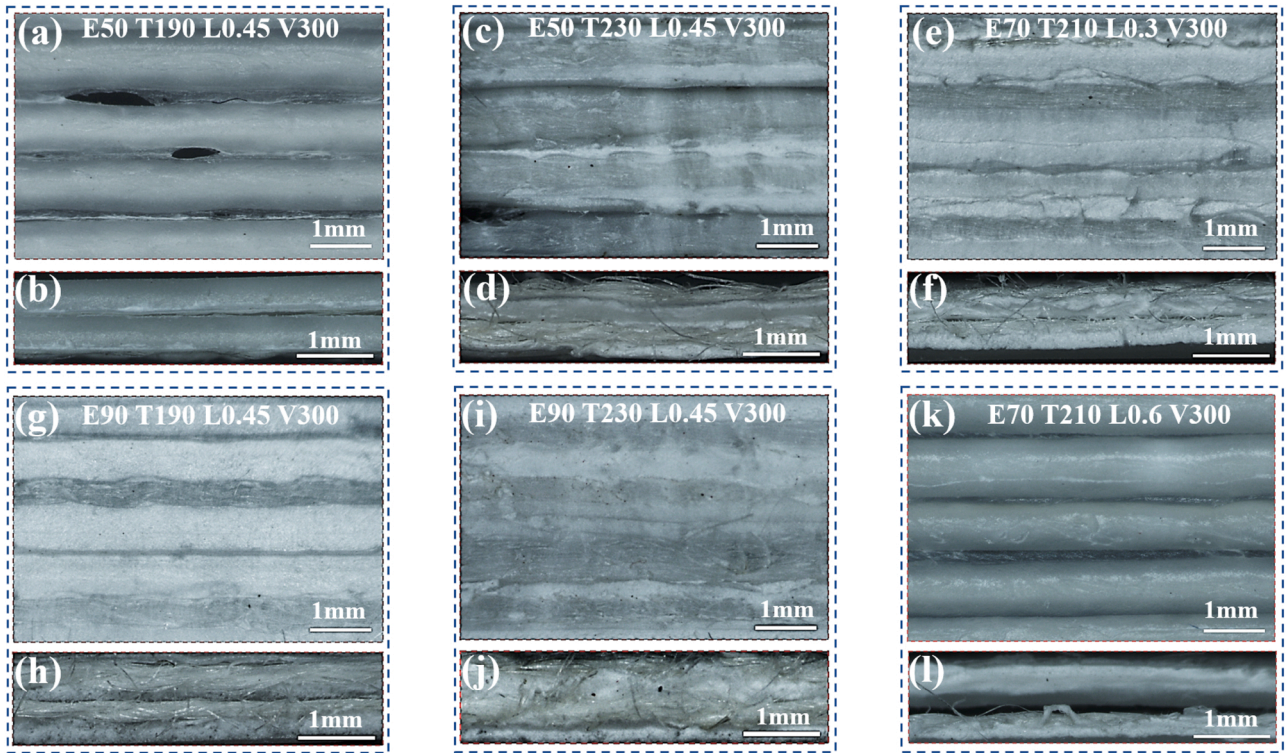

Fig. 9. Fracture surfaces of CRFRPP prepared under different printing parameters.

the fracture surface of CRFRPP with low printing temperature. In Fig. 9 (b), interlayer debonding can be seen in the fracture surface after Intra-Strength tests, indicating the bonding between layers was poor under low extrusion flow rate and low printing temperature. In addition, the fracture surface of CRFRPP with low extrusion flow rate and low printing temperature was smoother. A smooth surface means there are limited plastic deformations during debonding, indicating adhesion strength is poor. Similar results were also reported by Petersmann et al. [38]. Comparing Fig. 9(e) and (f) to Fig. 9(k) and (l), it can be found that the fracture surface became smoother as increasing the layer thickness. In addition, obvious interlayer debonding can be seen in the fracture surface after Intra-Strength test (Fig. 9(l)), which indicated the bonding between layers of CRFRPP was very poor at a high layer thickness. As a result, the Inter-Strengths of CRFRPP at higher layer thicknesses, lower extrusion flow rates and lower printing temperatures decreased significantly compared to those at lower layer thicknesses, higher extrusion flow rates and higher printing temperatures (see Figs. 3 and 5).

Factors such as matrix content, temperature and pressure during the forming process could affect the impregnation of fiber by resin and the microstructures such as pores and defects, thus affecting the interface properties of 3D-printed continuous fiber reinforced composites. Printing parameters in this study directly or indirectly affect the above factors and thus affect the Inter-Strength and Intra-Strength of CRFRPP. More specifically, increasing the extrusion flow rate could increase the matrix content, thus could (1) increase the contact pressure between extruded filaments and layers to promote better connections; (2) enable the fiber to be impregnated adequately by the matrix; and (3) enable more matrix flow into interlayer so to reduce the porosity, promoting better interface connection. Increasing the layer thickness could decrease forming pressure, which would increase the interface gap between deposited beams and layers, causing less interface interaction. Similar discussion can be found in Ref. [6]. Increasing the printing temperature could increase the fluidity of the matrix, which could (1) enable the matrix better impregnate the fiber; and (2) cause a lower ratio of deposited

filament height to width, resulting in a larger contact area between adjacent filament as reported by Ref. [15,37], causing more interfacial interaction. Vaes et al. [47] reported that as the printing temperatures increase, the interlayer bond strength of 3D-printed specimen increased since the weld time between layers increased. At high printing temperatures, the thermoplastic matrix had high fluidity, which made the deposited filaments more susceptible to small perturbation [15]. In addition, high printing speed could cause more perturbation of deposited filaments, which might result in defects between adjacent filaments in a layer. Therefore, the Intra-Strength of CRFRPP with high printing temperature decreased with the increase of printing speed (Fig. 5(d)).

4.3. Parameter optimization

As shown in Table 4, compared to CRFRPP with optimized parameters when Td was set at 90 %, Inter-Strength and Intra-Strength of CRFRPP with optimized parameters when Td was set at 80% decreased by 4 % and 12 %, respectively. However, its forming speed improved by 105 %. It can be seen that after parameter optimization, the strength was not reduced much while the forming efficiency was greatly improved. Therefore, in the actual production process, the optimization threshold can be set according to the actual needs, and then the parameters can be optimized based on the prediction results to ensure the strength of printed parts while improving the production efficiency and reducing costs. This could boost the wide application of 3D printing technology.

4.4. Interfacial properties and mechanical performance

To investigate how the difference in interfacial properties can be translated to the mechanical performance, bending tests were performed on printed specimens in directions perpendicular to the layers (out-of-plane) and parallel to the layers (in-plane). Fig. 10 shows the in-plane and out-of-plane flexural modulus and flexural strength of CRFRPP under different printing parameters. Note that the flexural properties at different printing speeds were not shown here because printing speed had insignificant effects on interfacial properties as stated above. And note that unmarked printing parameters are in the middle values in our study range. In Fig. 10, it seemed that the out-of-plane and in-plane flexural strength and modulus of the specimen did not present significant difference, which may be caused by a variety of reasons. This section focused on how the difference in interfacial properties influenced the mechanical performance, so the insignificant difference between the out-of-plane and in-plane flexural mechanical properties of the specimen was not discussed in detail. In addition, combining the results shown in Fig. 10 with those presented in Figs. 3 and 5, it could be found poor interface strengths resulted in inferior flexural properties.

In order to further explore how interfacial properties affect flexural mechanical properties of CRFRPP, the typical failure modes of specimens in bending tests are shown in Fig. 11. Note that only the failure behaviors of specimens with printing temperatures of 190 °C and 230 °C were shown here. For specimens with layer thickness of 0.6 mm and with extrusion flow rate of 50%, the failure behaviors were similar to the failure modes of specimens with printing temperatures of 190 °C. For specimens with layer thickness of 0.3 mm and with extrusion flow rate of 90 %, the failure behaviors were similar to the failure modes of specimens with printing temperatures of 230 °C, thus they were not shown here. In Fig. 11, it was observed that the specimen printed at 190 °C (which exhibited poor interfacial strengths) showed significant interlayer delamination during out-of-plane bending loading (see Fig. 11 (a)). In contrast, the specimen printed at 230 °C did not present delamination during the bending test, and their failure mode was the breakages of the fiber and matrix (see Fig. 11(b) and (d)). In addition, delamination was not seen on the front view of the specimen printed at 190 °C when subjected to in-plane bending load (see Fig. 11(c)). However, from the top view, the specimen printed at 190 °C exhibited significant interlayer delamination when subjected to in-plane bending load (see Fig. 11(e)). From the above results, it could be found that printed specimens with weak interfacial strength suffered interlaminar delamination failure when subjected to either in-plane or out-of-plane bending loads, leading to the ineffective load-bearing capacity of the fibers and matrix, thus greatly weakening the mechanical properties of the composites. In addition, delamination of adjacent printed filaments within a layer was not found when subjected to bending loads, which was because of the much higher Intra-Strength than Inter-Strength for printed samples with the same printing parameters (see Figs. 3 and 5).

5. Conclusion

In this study, the Inter-Strength and Intra-Strength of CRFRPP under different printing parameters were predicted by RSM and two ML methods: RF and ANN, based on the experimental data. Among the three methods, ANN showed the highest prediction accuracy, whereas RF presented acceptable accuracy while providing the importance of the parameters. The result of the importance of the parameters showed that extrusion flow rate had the most important influence on both Inter-Strength and Intra-Strength and printing speed presented a relatively small effect on the above two properties. More specifically, higher extrusion flow rates, lower layer thicknesses, and higher printing temperatures led to higher Inter-Strength and Intra-Strength of CRFRPP.

Moreover, the printing parameters were optimized based on the prediction. The optimization results suggested that the forming efficiency could increase significantly while the Inter-Strength and Intra-
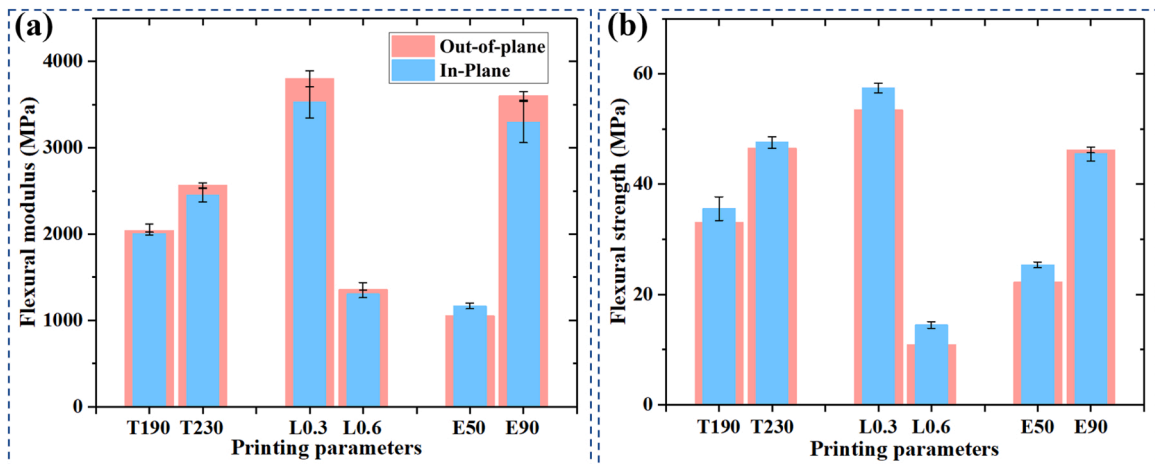

Fig. 10. (a) Flexural modulus and (b) flexural strength of CRFRPP under different printing parameters.
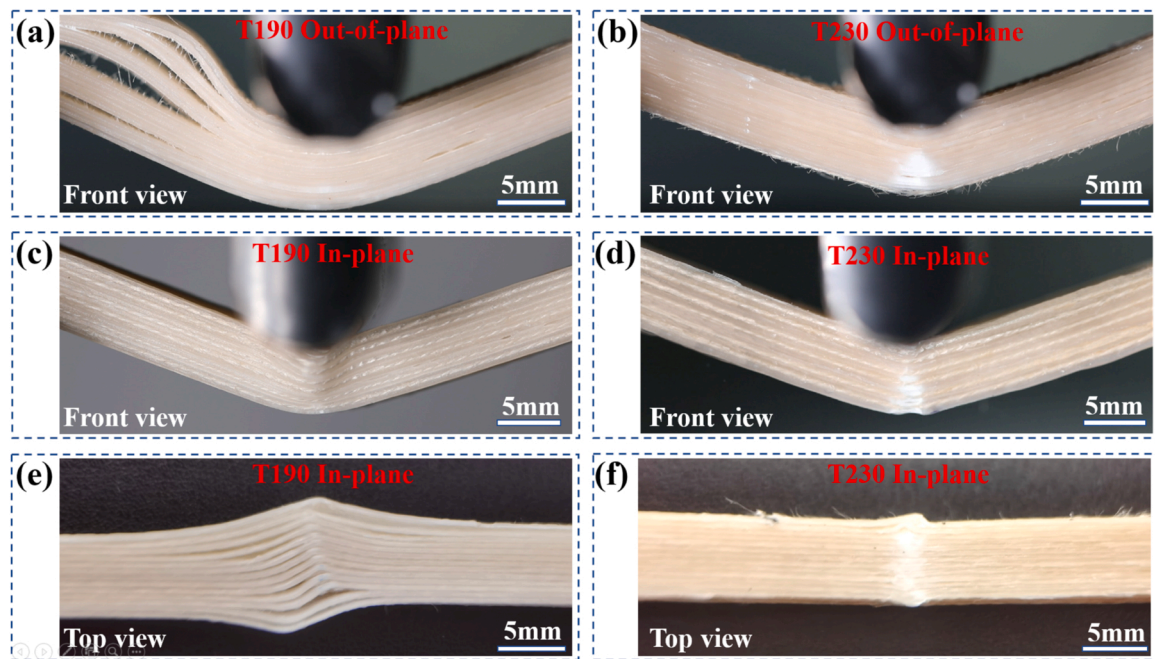
Fig. 11. Failure modes of specimens in bending tests under different printing parameters.

Strength of CRFRPP were not affected significantly. Therefore, based on the prediction results, the production efficiency of 3D-printed components could be improved using the proposed parameter optimization procedure and ensuring the properties, boosting the industrial application of 3D-printed products. Furthermore, the bending tests were carried out to investigate the effects of interfacial properties on the mechanical performance. The results found that printed specimens with weak interfacial strength suffered interlaminar delamination failure during bending loading, which greatly weakened the mechanical properties of the CRFRPP.

In future work, the effects of more printing parameters (e.g., platform temperature and print line spacing) and even environmental parameters (e.g., temperature and humidity of the printing chamber) on interfacial properties will be considered to study for achieving more precise and stable analysis results. In addition, more data preprocessing methods, training and test dataset preparation approaches and more ML methods will be attempted to establish more robust and more applicable models. Furthermore, material modification for increasing the interfacial reaction between the fiber and matrix using maleic anhydride grafted polypropylene and sodium hydroxide will be systematically studied.

CRediT authorship contribution statement

Ruijun Cai: Conceptualization, Methodology, Investigation, Formal analysis, Writing - Original Draft, **Wei Wen:** Conceptualization, Writing - Review & Editing, **Kui Wang:** Conceptualization, Methodology, Writing - Review & Editing, Supervision, Funding acquisition, **Yong Peng:** Resources, Project administration, **Said Ahzi:** Writing - Review & Editing **Francisco Chinesta:** Writing - Review & Editing, Validation.

Declaration of Competing Interest

The authors declare that they have no known competing financial interests or personal relationships that could have appeared to influence the work reported in this paper.

Appendix A. Supporting information

References

[1] S.A.M. Tofail, E.P. Koumoulos, A. Bandyopadhyay, S. Bose, L. O'Donoghue, C. Charitidis, Additive manufacturing: scientific and technological challenges, market uptake and opportunities, Mater. Today 21 (1) (2018) 22–37.

[2] X. Wang, M. Jiang, Z. Zhou, J. Gou, D. Hui, 3D printing of polymer matrix composites: a review and prospective, Compos. Part B 110 (2017) 442–458.

[3] P.K. Penumakala, J. Santo, A. Thomas, A critical review on the fused deposition modeling of thermoplastic polymer composites, Compos. Part B 201 (2020), 108336.

[4] N. van de Werken, H. Tekinalp, P. Khanbolouki, S. Ozcan, A. Williams, M. Tehrani, Additively manufactured carbon fiber-reinforced composites: state of the art and perspective, Addit. Manuf. 31 (2020), 100962.

[5] K. Wang, S. Li, Y. Wu, Y. Rao, Y. Peng, Simultaneous reinforcement of both rigidity and energy absorption of polyamide-based composites with hybrid continuous fibers by 3D printing, Compos. Struct. 267 (2021), 113854.

[6] P. Cheng, K. Wang, X. Chen, J. Wang, Y. Peng, S. Ahzi, C. Chen, Interfacial and mechanical properties of continuous ramie fiber reinforced biocomposites fabricated by in-situ impregnated 3D printing, Ind. Crops Prod. 170 (2021), 113760.

[7] G.D. Goh, Y.L. Yap, S. Agarwala, W.Y. Yeong, Recent progress in additive manufacturing of fiber reinforced polymer composite, Adv. Mater. Technol. 4 (1) (2019), 1800271.

[8] H.J. Aida, R. Nadlene, M.T. Mastura, L. Yusriah, D. Sivakumar, R.A. Ilyas, Natural fibre filament for fused deposition modelling (FDM): a review, Int. J. Sustain. Eng. 14 (6) (2021) 1988–2008.

[9] A. Pappu, K.L. Pickering, V.K. Thakur, Manufacturing and characterization of sustainable hybrid composites using sisal and hemp fibres as reinforcement of poly (lactic acid) via injection moulding, Ind. Crops Prod. 137 (2019) 260–269.

[10] R. Matsuzaki, M. Ueda, M. Namiki, T.-K. Jeong, H. Asahara, K. Horiguchi, T. Nakamura, A. Todoroki, Y. Hirano, Three-dimensional printing of continuous-fiber composites by in-nozzle impregnation, Sci. Rep. 6 (1) (2016) (23058).

[11] A. Le Duigou, A. Barbé, E. Guillou, M. Castro, 3D printing of continuous flax fibre reinforced biocomposites for structural applications, Mater. Des. 180 (2019), 107884.

[12] A. Le Duigou, G. Chabaud, R. Matsuzaki, M. Castro, Tailoring the mechanical properties of 3D-printed continuous flax/PLA biocomposites by controlling the slicing parameters, Compos. Part B 203 (2020), 108474.

[13] F.-L. Jin, R.-R. Hu, S.-J. Park, Improvement of thermal behaviors of biodegradable poly(lactic acid) polymer: a review, Compos. Part B 164 (2019) 287–296.

[14] X. Wang, S. Peng, H. Chen, X. Yu, X. Zhao, Mechanical properties, rheological behaviors, and phase morphologies of high-toughness PLA/PBAT blends by in-situ reactive compatibilization, Compos. Part B 173 (2019), 107028.

[15] K. Wang, R. Cai, Z. Zhang, J. Liu, S. Ahzi, Y. Peng, Y. Rao, Compressive behaviors of 3D printed polypropylene-based composites at low and high strain rates, Polym. Test. 103 (2021), 107321.

[16] M. Spoerk, F. Arbeiter, I. Ragv~, C. Holzer, J. Gonzalez-Gutierrez, Mechanical recyclability of polypropylene composites produced by material extrusion-based additive manufacturing, Polymers 11 (2019).

[17] B.A. Moore, E. Rougier, D. O'Malley, G. Srinivasan, A. Hunter, H. Viswanathan, Predictive modeling of dynamic fracture growth in brittle materials with machine learning, Comput. Mater. Sci. 148 (2018) 46–53.

[18] F. Wang, J. Wu, L. Hu, C. Yu, B. Wang, X. Huang, K. Miller, A. Wittek, Evaluation of the head protection effectiveness of cyclist helmets using full-scale computational biomechanics modelling of cycling accidents, J. Saf. Res. 80 (2022) 109–134.

[19] R. Cai, K. Wang, W. Wen, Y. Peng, M. Baniassadi, S. Ahzi, Application of machine learning methods on dynamic strength analysis for additive manufactured polypropylene-based composites, Polym. Test. 110 (2022), 107580.

[20] N. Wei, S. Yao, Y. Rao, K. Wang, Y. Peng, An integrated prediction model for processing related yield strength of extrusion-based additive manufactured polymers, Mech. Adv. Mater. Struct. (2022) 1–11.

[21] A.K. Sood, R.K. Ohdar, S.S. Mahapatra, Experimental investigation and empirical modelling of FDM process for compressive strength improvement, J. Adv. Res. 3 (1) (2012) 81–90.

[22] C. Wang, X.P. Tan, S.B. Tor, C.S. Lim, Machine learning in additive manufacturing: state-of-the-art and perspectives, Addit. Manuf. 36 (2020), 101538.

[23] O.A. Mohamed, S.H. Masood, J.L. Bhowmik, Investigation of dynamic elastic deformation of parts processed by fused deposition modeling additive manufacturing, Adv. Prod. Eng. Manag. 11 (3) (2016) 227–238.

[24] Ö. Bayraktar, G. Uzun, R. Çakiroğlu, A. Guldas, Experimental study on the 3D-printed plastic parts and predicting the mechanical properties using artificial neural networks, Polym. Adv. Technol. 28 (8) (2017) 1044–1051.

[25] A. Douard, C. Grandvallet, F. Pourroy, F. Vignat, An Example of Machine Learning Applied in Additive Manufacturing, In: Proceedings of the 2018 IEEE International Conference on Industrial Engineering and Engineering Management (IEEM), 2018, pp. 1746–1750.

[26] K. Aoyagi, H. Wang, H. Sudo, A. Chiba, Simple method to construct process maps for additive manufacturing using a support vector machine, Addit. Manuf. 27 (2019) 353–362.

[27] S. Wang, Y. Ma, Z. Deng, S. Zhang, J. Cai, Effects of fused deposition modeling process parameters on tensile, dynamic mechanical properties of 3D printed polylactic acid materials, Polym. Test. 86 (2020), 106483.

[28] S.M.F. Kabir, K. Mathur, A.-F.M. Seyam, A critical review on 3D printed continuous fiber-reinforced composites: history, mechanism, materials and properties, Compos. Struct. 232 (2020), 111476.

[29] M.A. Caminero, J.M. Chacón, I. García-Moreno, J.M. Reverte, Interlaminar bonding performance of 3D printed continuous fibre reinforced thermoplastic composites using fused deposition modelling, Polym. Test. 68 (2018) 415–423.

[30] T. Liu, X. Tian, M. Zhang, D. Abliz, D. Li, G. Ziegmann, Interfacial performance and fracture patterns of 3D printed continuous carbon fiber with sizing reinforced PA6 composites, Compos. Part A 114 (2018) 368–376.

[31] Y. Wu, K. Wang, V. Neto, Y. Peng, R. Valente, S. Ahzi, Interfacial behaviors of continuous carbon fiber reinforced polymers manufactured by fused filament fabrication: a review and prospect, Int. J. Mater. Form. 15 (3) (2022) 18.

[32] S. Li, K. Wang, W. Zhu, Y. Peng, S. Ahzi, F. Chinesta, Contributions of interfaces on the mechanical behavior of 3D printed continuous fiber reinforced composites, Constr. Build. Mater. 340 (2022), 127842.

[33] D. Yavas, Z. Zhang, Q. Liu, D. Wu, Interlaminar shear behavior of continuous and short carbon fiber reinforced polymer composites fabricated by additive manufacturing, Compos., Part B 204 (2021), 108460.

[34] S. Beg, S. Akhter, Box–Behnken designs and their applications in pharmaceutical product development, in: S. Beg (Ed.), Design of Experiments for Pharmaceutical Product Development: Volume I: Basics and Fundamental Principles, Springer Singapore, Singapore, 2021, pp. 77–85.

[35] S. Zhang, Y. Sun, Y. Cheng, P. Huang, M.O. Oladokun, Z. Lin, Response-surface-model-based system sizing for Nearly/Net zero energy buildings under uncertainty, Appl. Energy 228 (2018) 1020–1031.

[36] X. Shen, G. Zhang, B. Bjerg, Assessments of experimental designs in response surface modelling process: estimating ventilation rate in naturally ventilated livestock buildings, Energy Build. 62 (2013) 570–580.

[37] S. Charlon, J. Le Boterff, J. Soulestin, Fused filament fabrication of polypropylene: influence of the bead temperature on adhesion and porosity, Addit. Manuf. 38 (2021), 101838.

[38] S. Petersmann, P. Spoerk-Erdely, M. Feuchter, T. Wieme, F. Arbeiter, M. Spoerk, Process-induced morphological features in material extrusion-based additive manufacturing of polypropylene, Addit. Manuf. 35 (2020), 101384.

[39] M.V. Candal, I. Calafel, N. Aranburu, M. Fernández, G. Gerrica-Echevarria, A. Santamaría, A.J. Müller, Thermo-rheological effects on successful 3D printing of biodegradable polyesters, Addit. Manuf. 36 (2020), 101408.

[40] M.V. Candal, I. Calafel, M. Fernández, N. Aranburu, R.H. Aguirresarobe, G. Gerrica-Echevarria, A. Santamaría, A.J. Müller, Study of the interlayer adhesion and warping during material extrusion-based additive manufacturing of a carbon nanotube/biobased thermoplastic polyurethane nanocomposite, Polymer 224 (2021), 123734.

[41] C.S. Davis, K.E. Hillgartner, S.H. Han, J.E. Seppala, Mechanical strength of welding zones produced by polymer extrusion additive manufacturing, Addit. Manuf. 16 (2017) 162–166.

[42] J.E. Seppala, S. Hoon Han, K.E. Hillgartner, C.S. Davis, K.B. Migler, Weld formation during material extrusion additive manufacturing, Soft Matter 13 (38) (2017) 6761–6769.

[43] E. Barocio, B. Brenken, A. Favaloro, R.B. Pipes, Interlayer fusion bonding of semi-crystalline polymer composites in extrusion deposition additive manufacturing, Compos. Sci. Technol. (2022), 109334 in press.

[44] F. Pedregosa, G. Varoquaux, A. Gramfort, V. Michel, B. Thirion, O. Grisel, M. Blondel, P. Prettenhofer, R. Weiss, V. Dubourg, Scikit-learn: machine learning in python, J. Mach. Learn. Res. 12 (2011) 2825–2830.

[45] M.A. Mahmood, A.I. Visan, C. Ristoscu, I.N. Mihailescu, Artificial neural network algorithms for 3D printing, Materials 14 (1) (2021) 163.

[46] Z. Zhang, Artificial Neural Network, Multivariate Time Series Analysis in Climate and Environmental Research, Springer, 2018, pp. 1–35.

[47] D. Vaes, M. Coppens, B. Goderis, W. Zoetelief, P. Van Puyvelde, The extent of interlayer bond strength during fused filament fabrication of nylon copolymers: an interplay between thermal history and crystalline morphology, Polymers 13 (16) (2021) 2677.